ORIGINAL RESEARCH ARTICLE

Role of Dislocations and Interfaces on the Nanoscale Random Precipitation Kinetics in Vanadium-Alloyed Steels Studied by SANS

ZAMRAN ZAHOOR KHAN, AMIR SABET GHORABAEI, SONIA GUEHAIRIA, STEVEN R. PARNELL, DIRK HONECKER, PETER HEDSTRÖM, BART J. KOOI, S. ERIK OFFERMAN, and NIELS H. VAN DIJK

This study uses small-angle neutron scattering (SANS) to investigate vanadium carbide (VC) random precipitation (RP) kinetics in two nanosteels with varying vanadium and carbon contents during aging for up to 10 hours at 600 and 650 °C. Starting from a martensitic microstructure, the evolution of the VC precipitate size distributions is tracked over time. Atom probe tomography (APT) and scanning transmission electron microscopy (STEM) provide complementary characterization of precipitate shape, morphology, and composition. The precipitation process follows a sequence of burst nucleation, rapid growth, and coarsening, driven by enhanced diffusion along dislocations and interfaces. VC precipitates form primarily at martensitic interfaces, adopting predominantly oblate ellipsoidal particles. Analysis of the time-dependent precipitate size indicates that pipe diffusion along dislocations is the dominant diffusion mechanism during coarsening. Using the Ashby-Orowan model, we estimate the strength enhancement from VC precipitation. Maximum VC strengthening occurs at different aging times depending on steel composition. For steels with a high carbon and vanadium content, peak strengthening occurs after 120 minutes of aging at 650 °C. Reducing the carbon and vanadium content prolongs the time required to reach peak strengthening, extending it to 300 minutes at 650 °C. The nuclear-to-magnetic scattering ratio shows a time-dependent evolution indicating a temporal compositional change in the VC precipitates during aging.

The handling Editor for this article is Matthias Militzer.

ZAMRAN ZAHOOR KHAN and NIELS H. VAN DIJK are with the Department of Radiation Science and Technology, Delft University of Technology, Mekelweg 15, 2629 JB Delft, The Netherlands. Contact e-mail: z.z.khan@tudelft.nl AMIR SABET GHORABAEI and BART J. KOOI are with the Zernike Institute for Advanced Materials, University of Groningen, Nijenborgh 3, 9747 AG Groningen, The Netherlands. SONIA GUEHAIRIA and PETER HEDSTRÖM are with the Department of Materials Science and Engineering, Unit of Hultgren Laboratory, KTH Royal Institute of Technology, Brinellvägen 23, SE-100 44 Stockholm, Sweden. STEVEN R. PARNELL and DIRK HONECKER are with the ISIS Pulsed Neutron and Muon Source, Rutherford Appleton Laboratory, Chilton, Didcot, Oxfordshire, OX11 0QX, UK. S. ERIK OFFERMAN is with the Department of Materials Science and Engineering, Delft University of Technology, Mekelweg 2, 2628 CD Delft, The Netherlands.
Manuscript submitted February 24, 2026; accepted June 6, 2026.

Published online: 11 July 2026

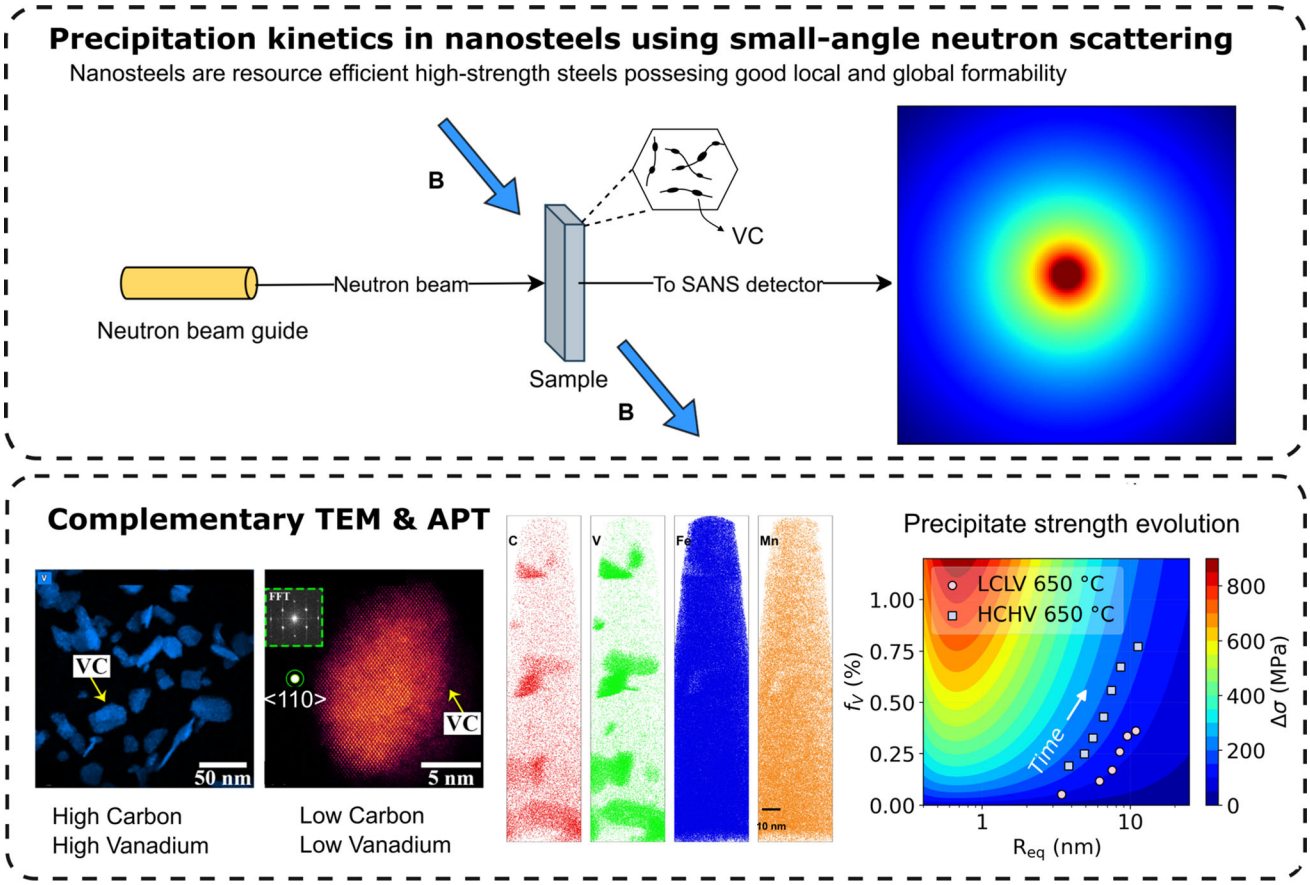

https://doi.org/10.1007/s11661-026-08288-8

I. INTRODUCTION

NANOSTEELS are a new generation of advanced high-strength steels (AHSS) possessing a desirable combination of properties, *i.e.,* high strength and good global and local formability, while being resource efficient at the same time.[1] These steels derive their exceptional properties from the nanoscale precipitates, which are formed by the addition of micro-alloying elements like vanadium, titanium, molybdenum and niobium.[2] The nanoscale precipitates can form in both single-phase and multi-phase variants of ferritic, bainitic, and martensitic steels.[1–5] The combination of high strength provided by the precipitates and ductility provided by the matrix makes these steels a good candidate for manufacturing lightweight and intricate automobile components like the chassis. This is of particular interest to the electric vehicle (EV) industry, as using these steels would increase the miles per gallon of gasoline-equivalent (MPGe) *via* vehicle weight reduction, while simultaneously preserving crashworthiness.[6]

The precipitates can form through various precipitation mechanisms that influence the steel's properties. Of particular importance is the steel's strength, which is determined by the precipitate volume fraction, size distribution, composition, and morphology.[7–9] These precipitates obstruct the movement of dislocations when the steel is under external load, resulting in an increase in strength. This is also known as precipitation strengthening.[7–9] The interaction of moving dislocations with the precipitates depends on the precipitate size, with the dislocations tending to cut through smaller precipitates and tending to bow around the larger ones.[7–9] To optimize the precipitate strengthening, a good control of the particle size and number density must be established, which can be achieved through the application of specific thermal treatments. Different thermal treatments result in either interphase precipitation (IP) or random precipitation (RP).[10]

IP involves the formation of nanoscale precipitates during the austenite-to-ferrite phase transformation. The precipitates are formed along the moving interface separating the high-temperature austenite phase from the lower-temperature ferrite phase.[11] The interphase precipitation kinetics are claimed to be controlled either by the solute drag effect[12] or by the pinning effect of the formed precipitates on the moving interface.[13] For steels with IP as the precipitation mechanism, an extremely high number density of precipitates has been

reported.[14,15] A recent in situ SANS study on IP, however, reports lower precipitate number density values.[16]

RP involves the formation of nanoscale precipitates during aging at elevated temperatures, primarily on preferred nucleation sites like dislocations and (sub)-grain boundaries [(S)GBs] throughout the matrix. The precipitation process involves the diffusion of solute atoms to the preferred nucleation sites. The diffusivities of the solute atoms toward these preferred nucleation sites, *i.e.,* pipe diffusion in dislocations and boundary diffusion in (S)GBs, are significantly higher than the volume diffusion in the matrix.[17,18] As the precipitate nucleation rate is proportional to the density of potential nucleation sites like dislocations,[19] a high density of dislocations would result in a high number density of the nanoscale precipitates, which ultimately results in a large strength enhancement. The martensitic phase transformation generates a high density of dislocations and (S)GBs, such as martensitic lath, block, and packet boundaries.[19] RP can be achieved by aging martensitic steels at elevated temperatures.

Vanadium micro-alloyed steels strengthened with vanadium carbide (VC) nanoprecipitates have gained increasing attention in recent years.[20–22] The formation of nanoscale VC precipitates depends on the steel's composition and on the applied heat treatment.[10,15,16] VC precipitates can form in different morphologies, including spheres and ellipsoids[10,16] and with different stoichiometries like VC, V_8C_7, and V_4C_3.[23–25] The incorporation of substitutional atoms like Fe has also been observed in VC precipitates formed through IP.[26] For IP, Ioannidou and coworkers[26] reported that the VC composition evolves with aging time with a transition from a core-shell structure to a homogeneous sphere for increasing aging times. However, for RP, the evolution in structure and composition of VC precipitates during the nucleation, growth and coarsening stages of the aging process remain unclear.

Previous studies have characterized the VC volume fraction and size distribution using (scanning) transmission electron microscopy (S/TEM).[27] While S/TEM provides an exceptional imaging resolution for the nanoscale precipitates, it presents two major limitations. First, S/TEM probes a very small sample volume, potentially giving statistically inadequate information. Second, using S/TEM to study the precipitation kinetics is experimentally demanding and time consuming. Atom probe tomography (APT) has also been employed to study VC precipitates, but faces similar challenges as S/TEM because of the limited sampling volume. Scattering techniques such as small-angle neutron scattering (SANS) and small-angle X-ray scattering (SAXS) have emerged as powerful non-destructive tools for monitoring the nanoscale (1 to 200 nm) precipitate size distribution and volume fraction during aging at elevated temperatures. These techniques provide statistically representative data on the precipitates and are suitable for kinetic studies.[8,28] The SANS technique has been successfully applied to study the VC interphase precipitation kinetics in vanadium micro-alloyed steels.[26]

In this work, for the first time, a time-dependent quantitative study on the random VC precipitation kinetics in martensitic nanosteels is performed using SANS to understand the interplay between nucleation, growth, and coarsening of the nanoscale precipitates with the dislocations and interfaces. The SANS results are complemented with the precipitate shape information from STEM and the composition information from APT. The random VC precipitation kinetics has been followed at two different aging temperatures of 600 °C and 650 °C and for aging times up to 600 minutes.

II. EXPERIMENTAL PROCEDURES

A. *Samples*

Rolled sheets of nanosteels with two different compositions referred to as low-carbon low-vanadium (LCLV) and high-carbon high-vanadium (HCHV) were produced at Tata Steel, IJmuiden, Netherlands. The chemical compositions of these LCLV and HCHV nanosteels are listed in Table I. Rectangular samples of dimensions 9.2 × 10 × 1.0 mm^3 were cut from the steel sheets by wire electrical discharge machining (EDM). The long axis of the rectangular samples coincides with the rolling direction of the as-received steel sheets.

B. *Thermal Treatments*

The LCLV and HCHV steel samples were heat treated in a dilatometer (Bähr-Thermoanalysis GmbH). The applied heat treatment aimed to induce random precipitation during aging can be seen in Fig. S1. The heat treatment involved heating the samples to 1100 °C for the HCHV alloy and 1050 °C for the LCLV alloy at a constant rate of 5 °C/s. The samples were then held at the selected temperatures for 15 minutes to dissolve any possible carbides and redistribute the micro-alloying elements homogeneously in the austenite matrix. After this step, the samples were quenched to room temperature at a cooling rate of about 500 °C/s to induce a martensitic phase transformation. To ensure that the specimen volume reached a fully martensitic microstructure with a high dislocation density, the samples were held at room temperature for a period of 20 s. Subsequently, the samples were rapidly heated up to aging temperatures of 600 °C and 650 °C at a rate of 50 °C/s to minimize the annihilation of the dislocations before the start of the aging period. The aging temperatures were selected to induce VC precipitation in accordance with the predictions from Thermo-Calc phase equilibrium calculations (Fig. S2). After heating to the selected aging temperature, the samples were held for different aging times (2, 5, 10, 20, 45, 120, 300 and 600 minutes) and then quenched back to room temperature. The dilatometry data for the heat treatment were analyzed using Python routines.

C. *SANS Measurements*

Room-temperature SANS experiments were performed on the heat-treated samples. This was done on the LARMOR instrument at the ISIS Pulsed Neutron and Muon Source, RAL, UK. A neutron beam of 5×5 mm^2, with a wavelength ranging from 4.2 to 13 Å, was used. The lowest value of the wavelength range was chosen to avoid multiple Bragg scattering. The ferromagnetic samples were measured in a magnetic field of 1.65 T, which was applied perpendicular to the direction of the neutron beam and along the rolling direction of the samples. The applied magnetic field that magnetically saturates the ferromagnetic matrix gives rise to anisotropic scattering, enabling the separation between nuclear and magnetic scattering. The run time for each sample measurement was $\sim$ 1 hour. The raw scattering patterns were corrected for sample transmission and background.[29] The SANS data reduction was performed using the Mantid software,[30] and the SANS data analysis and fitting were performed using the SASview software.[31]

SANS is a powerful, non-destructive technique used to study nanometre dimensioned structures, ranging from 1 to 200 nm. In this technique, a neutron beam is directed toward the sample which then scatters off the objects present in the bulk of the sample at small angles. This scattering gives rise to an interference pattern, which contains information on the different scatterers present in the sample.

The scattering can be of two types, nuclear and magnetic. Nuclear scattering involves neutrons that interact with atomic nuclei and is sensitive to compositional variations in the sample. These variations give rise to a nuclear neutron contrast $\Delta\rho^2_{nuc}$, which is the square of the difference in the scattering length densities of the VC precipitates and the Fe matrix. Based on compositional input on the VC precipitates from equilibrium calculations performed in Thermo-Calc (Fig. S2), the theoretical nuclear contrast was calculated to be $\Delta\rho^2_{nuc} = 20.69 \times 10^{28}\text{m}^{-4}$, using the same method as was used in previous work.[10] Magnetic scattering involves neutrons that interact with magnetic moments of unpaired electrons, probing magnetic structures present in the sample. The magnetic contrast between the ferromagnetic BCC Fe matrix and the paramagnetic VC precipitates was calculated to be $\Delta\rho^2_{mag} = 24.59 \times 10^{28}\text{m}^{-4}$ at room temperature.[10]

To separate magnetic from nuclear scattering, the ferromagnetic sample, while being exposed to the neutron beam, was placed in an external magnetic field B of strength 1.65T. This magnetically saturates the sample by aligning the magnetic moments in the direction of the external magnetic field, resulting in anisotropic neutron scattering described by the following equation

$$I(Q) = I(Q)_{\text{nuc}} + I(Q)_{\text{mag}} \sin^2 \alpha \qquad [1]$$

where $I(Q)$ is the total differential scattering cross section [cm^{-1}], $I(Q)_{nuc}$ is the nuclear differential scattering cross section and $I(Q)_{mag}$ is the magnetic differential scattering cross section. The wave-vector transfer [Å^{-1}] corresponds to $= |\text{Q}| = (4\pi/\lambda)\sin\theta$, where θ is half the scattering angle. The angle α corresponds to the angle between the wave-vector transfer Q and the external magnetic field B.

To validate the magnetic saturation in the studied samples, SANS measurements as a function of magnetic field strength were performed. For small fields (< 0.5 T) the total SANS is found to reduce strongly with increasing magnetic field strength as the magnetic domain structure is transformed into a single magnetic domain of the entire ferromagnetic matrix (Fig. S3). For larger fields, the total SANS signal approaches a minimum. The maximum applied magnetic field of 1.65 T is found to be sufficiently large to ensure magnetic saturation. The 2D SANS patterns obtained without magnetic field and with an external magnetic field of 1.65 T can be seen in Fig. S3.

It now becomes possible to extract the 1D radially averaged $I(Q)$ *vs* Q plots from these 2D SANS patterns. This is done by integrating sectors of 30 deg, parallel ($\alpha = -15$ deg to 15 deg and 165 deg to 195 deg) and perpendicular ($\alpha = 75$ deg to 105 deg and 255 deg to 285 deg) to the direction of the external magnetic field. The sectors parallel to the magnetic field contain contribution from the nuclear SANS, $I(Q)_{nuc}$, whereas the sectors perpendicular to the magnetic field contain contributions from both the nuclear and magnetic SANS, $I(Q)_{nuc} + I(Q)_{mag}$. Subtracting the former from the later yields the magnetic SANS, $I(Q)_{mag}$.

The kinetics of nanoscale VC precipitation is studied using SANS by extracting the precipitate size distribution and volume fraction from each measured sample. One major advantage of using SANS is that it probes a large sample volume, giving statistically representative information. Complementary techniques like S/TEM and APT are used to provide detailed information on the precipitate shape and chemistry from a much smaller sample volume.

D. *SEM and TEM Measurements*

A microstructural analysis of the heat-treated LCLV and HCHV samples was performed, including specimens that were quenched immediately after austenitization. The specimens were prepared by standard grinding and polishing by a 1 μm diamond suspension, followed by etching with a 2 pct Nital solution for about 10 to 12 s prior to general microstructural examinations. Scanning electron microscopy (SEM) was performed at an accelerating voltage of 20 kV using a JEOL JSM-6500F microscope.

To investigate the shape and morphology of VC nanoprecipitates, carbon extraction replicas (CERs) were prepared according to an optimized procedure.[32] The CERs were studied using a TFS Titan Themis Z probe and image aberration-corrected S/TEM equipped with a dual-X energy-dispersive X-ray spectroscopy (EDS) detector at an accelerating voltage of 300 kV. High-angle annular dark-field (HAADF-STEM) imaging was performed using a convergence semi-angle of 18.0 mrad, a probe current of about 25 or 150 pA, and a

Table I. Chemical Compositions of the LCLV and HCHV Alloys with Balance Fe

Steel		C	Si	Mn	S	Cr	Mo	Al	Nb	V
LCLV	wt pct	0.068	0.008	1.790	0.001	0.001	0.002	0.035	0.001	0.285
	at pct	0.315	0.016	1.813	0.002	0.001	0.001	0.072	0.0006	0.311
HCHV	wt pct	0.138	0.011	1.790	0.001	0.002	0.002	0.036	< 0.001	0.609
	at pct	0.638	0.022	1.808	0.002	0.002	0.001	0.074	< 0.0006	0.663

HAADF detector collection angle range of 43 to 200 mrad at a camera length of 115 mm. EDS spectrum imaging was carried out at a probe current of about 500 pA.

E. *APT Measurements*

APT needle-shaped specimens were prepared from the LCLV and HCHV samples after 5 hours aging at 650 °C to determine the chemical composition of the matrix and nanoscale precipitates. The specimens were designed using a Helios 5 UC dual-beam SEM–FIB system following conventional lift-out and annular milling procedures.[33] Final tip sharpening was performed at 30 kV and 24 pA, followed by a low-energy cleaning step at 5 kV and 41 pA to remove the protective Pt layer and refine the apex geometry while minimizing Ga ion-induced surface damage.[34,35]

APT analyses were conducted under ultra-high vacuum on a CAMECA EIKOS-UV instrument equipped with a 355 nm UV laser. The lase mode was employed with a pulse energy of 20 nJ, a repetition rate of 200 kHz, and a temperature of 50 K. The detection rate was maintained between 0.3 and 0.4 pct to ensure stable field evaporation and optimal mass resolution. The cryogenic environment ensured apex stability and minimized surface diffusion during data acquisition.[36–38]

Three-dimensional reconstructions were performed using the 3Depict software[39] and quantitative compositional analyses were carried out using APSuite (version 6.3.1.110). Concentration proximity histograms (proxigrams) were generated using the V iso-concentration surface at 2.5 at pct as a reference to characterize the VC-rich precipitates as a function of the distance from the precipitate–matrix interface. The proxigram approach enables direct visualization of compositional gradients across the interface and quantitative determination of precipitate size, composition, and volume fraction.[40,41]

F. *Hardness Measurements*

Vickers hardness tests were performed on the heat-treated LCLV and HCHV samples using a hardness testing machine (Struers DuraScan 20) with a load of 5 kgf and a loading period of about 30 s for each measurement. The samples were prepared by grinding to 2000-grit sandpaper and subsequently cleaned with isopropanol prior to testing. An average of three to four measurements was considered for each sample.

III. RESULTS

A. *Characterization of the Microstructure*

The SEM images in Figures 1(a) and (b) show fully martensitic microstructures in the samples that are quenched after austenitization. The fraction of austenite transformed into martensite during quenching can be seen in Fig. S4. Achieving a fully martensitic microstructure before aging is important to optimize the RP mechanism. Martensite contains a high density of interfaces and dislocations, which both act as preferred nucleation sites for the VC precipitate formation. Typical microstructures of the aged samples can be seen in Figures 1(c) and (d). The prior austenite grains are visible in these aged samples. After a prolonged aging period of 600 minutes at 650 °C, the martensite morphology is still clearly visible, indicating strong tempering resistivity of the studied alloys. The zoomed-in region in Figure 1(d) highlights a martensitic interface (indicated by the yellow arrow), characteristic for the martensitic matrix.

Figures 2(a) and (d) show the distribution of precipitates in the CERs of the LCLV and HCHV alloy samples aged for 600 minutes at 650 °C. Qualitatively, the HCHV alloy sample exhibits a higher precipitate number density than the LCLV alloy sample. The precipitates are predominantly oblate ellipsoidal in shape and form randomly within the martensitic substructure. Coarser nanoprecipitates decorate subgrain boundaries (SGBs) [Figures 2(b) and (e)], whereas finer ones are distributed within the martensite laths [Figures 2(c) and (f)]. The oblate ellipsoidal morphology arises from a combination of thermodynamic and kinetic factors. From a kinetic perspective, TEM observations in the present work indicate preferential nucleation of VC precipitates at martensitic interfaces. Such interfaces are known to provide enhanced solute transport pathways, which can promote lateral growth along the interface plane and contribute to the development of an oblate morphology. The precipitates are identified as vanadium carbides with a rock-salt crystal structure [Figures 2(g) and (h)]. Both alloys show similar VC precipitate size distributions after prolonged aging for 600 minutes at 650 °C, with mean diameters of 22 and 19 nm for the LCLV and HCHV alloy samples, respectively [Figures 2(i) and (j)].

The spatial distribution of the main elements within the HCHV and LCLV samples after 5 hours of aging at 650 °C is illustrated in Figures 3(a) and (c). This specific aging condition (5 hours at 650 °C) was selected for APT analysis to ensure the presence of VC precipitates

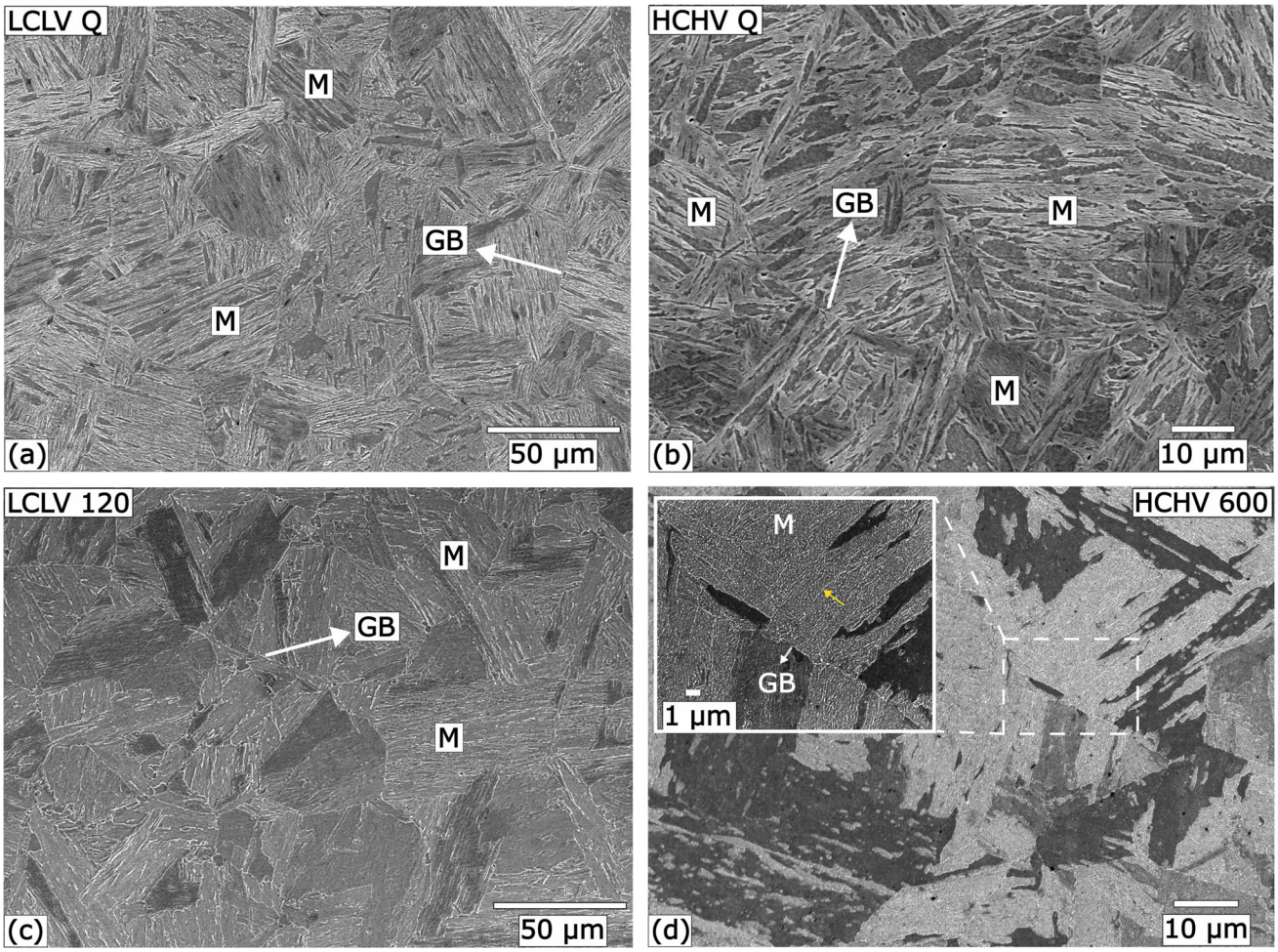

Fig. 1—SEM micrographs (taken with a secondary-electrons detector) showing the microstructures in the LCLV and HCHV alloy samples. (*a*) LCLV alloy in the as-quenched condition after austenitization. (*b*) HCHV alloy in the as-quenched condition after austenitization. The quenched alloys show fully martensitic microstructures. (*c*) LCLV alloy after aging for 120 min at 650 °C. (*d*) HCHV alloy after aging for 600 min at 650 °C. Martensitic morphology retained after prolonged aging periods. M: martensite, GB: grain boundary.

in the samples. Additionally, longer aging enables an approach to the thermodynamic equilibrium conditions (Figure S2). The 3D reconstructions show that carbon (red) and vanadium (green) are concentrated in nanoscale regions corresponding to V-C-rich precipitates, whereas iron (blue) and manganese (orange) remain homogeneously distributed within the matrix. The iso-concentration surface of 2.5 pct V reveals the morphology and spatial distribution of these precipitates within the analyzed volume. The co-localization of vanadium and carbon clearly indicates the formation of vanadium carbides (VC) with oblate ellipsoid morphologies during annealing, confirming the previous STEM observations [Figures 2, 3(a) and (c)]. Figures 3(b) and (d) show proxigrams illustrating the variation in chemical composition with the distance from the matrix–precipitate interface. The precipitates are primarily composed of V, C, and Fe Table II. The detection of Fe in the VC precipitates is consistent with the thermodynamic equilibrium calculations [see Figure S.2 (d)].

B. *Effect of VC Precipitation on the Hardness*

Upon aging, the martensitic starting microstructure provides a high density of potential nucleation sites for VC precipitate formation in the form of dislocations and subgrain boundaries. It is expected that during aging, fast initial nucleation of precipitates is followed by growth and coarsening. In the absence of precipitation, the martensitic matrix would be expected to soften progressively during aging due to two mechanisms: grain coarsening and dislocation annihilation. The former leads to a reduction in grain boundary strengthening, which scales with grain size according to the Hall–Petch relationship, $\Delta\sigma_{GB} \propto 1/\sqrt{d_g}$, where d_g is the average grain size. The latter results in a reduction in dislocation strengthening, which scales as $\Delta\sigma_d = M\alpha Gb\rho^{1/2}$, where M is the Taylor factor, α is a constant, G is the shear modulus, b is the Burgers vector, and ρ is the dislocation density. Öhlund *et al.*[42] reported that the dislocation density decreases approximately by a factor of twelve within the first 150 s of annealing at 550 °C of a Ti-containing martensitic steel (0.39 wt pct C, 0.04 wt pct Ti) containing TiC

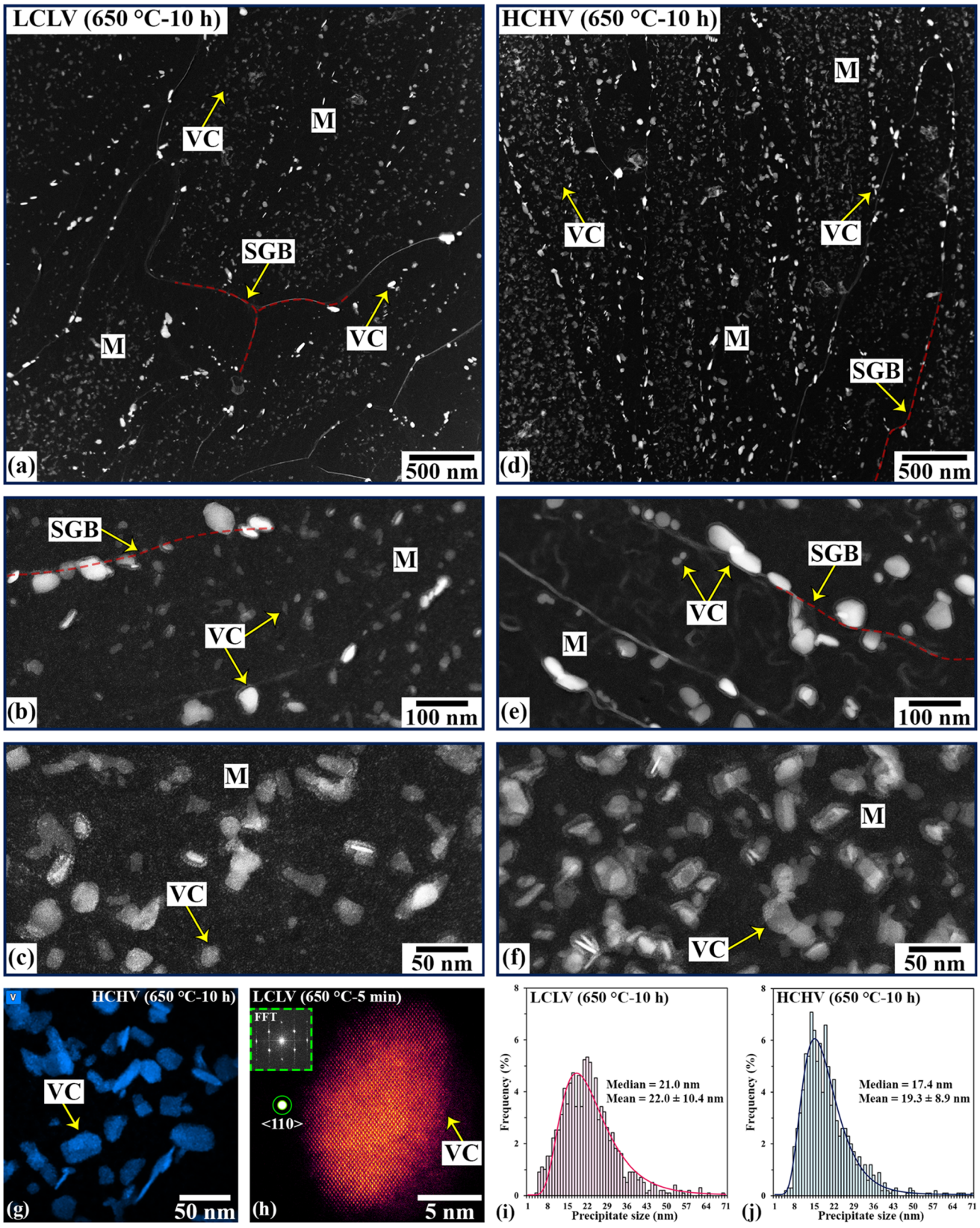
LCLV (650 °C-10 h)
VC
M
SGB
M
VC
(a)
500 nm
HCHV (650 °C-10 h)
M
VC
VC
M
SGB
(d)
500 nm
SGB
M
VC
(b)
100 nm
SGB
VC
M
(e)
100 nm
M
VC
(c)
50 nm
M
VC
(f)
50 nm
HCHV (650 °C-10 h)
VC
(g)
50 nm
LCLV (650 °C-5 min)
FFT
<110>
VC
(h)
5 nm
LCLV (650 °C-10 h)
Median = 21.0 nm
Mean = 22.0 ± 10.4 nm
Frequency (%)
Precipitate size (nm)
(i)
HCHV (650 °C-10 h)
Median = 17.4 nm
Mean = 19.3 ± 8.9 nm
Frequency (%)
Precipitate size (nm)
(j)

◀Fig. 2—STEM analysis of CERs for the selected LCLV and HCHV samples. (*a*) through (*c*) and (*d*) through (*f*) Typical HAADF-STEM images of random VC nanoprecipitates in the LCLV and HCHV samples aged for 600 min at 650 °C, respectively. (*g*) EDS spectrum image from the HCHV (650 °C-10 h) CER showing the vanadium concentration map, acquired using the K_α X-ray peak. (*h*) Atomic-resolution HAADF-STEM image of a VC nanoprecipitate viewed along the ⟨110⟩ zone axis from the LCLV (650 °C-5 min) CER. The inset shows the corresponding fast Fourier transform (FFT) image. (*i*) and (*j*) Log-normal size distributions for random VC nanoprecipitates in the LCLV and HCHV (650 °C-10 h) CERs, respectively, determined from manual measurements of about 1000 precipitates per sample. M: martensite, VC: vanadium carbide, SGB: subgrain boundary.

nanoprecipitates, illustrating how rapidly this softening mechanism can operate.

Despite the expected softening by recovery, the hardness data presented in Figure 4 show a slight increase with aging time in both alloys. This behavior indicates that precipitation strengthening from VC largely compensates the concurrent loss in strength by the reduction in dislocations and grain boundaries and is therefore a significant contributor to the overall strength evolution during aging. The fact that the hardness increases rather than decreases during early to intermediate aging times, despite the operation of recovery mechanisms, provides indirect but meaningful

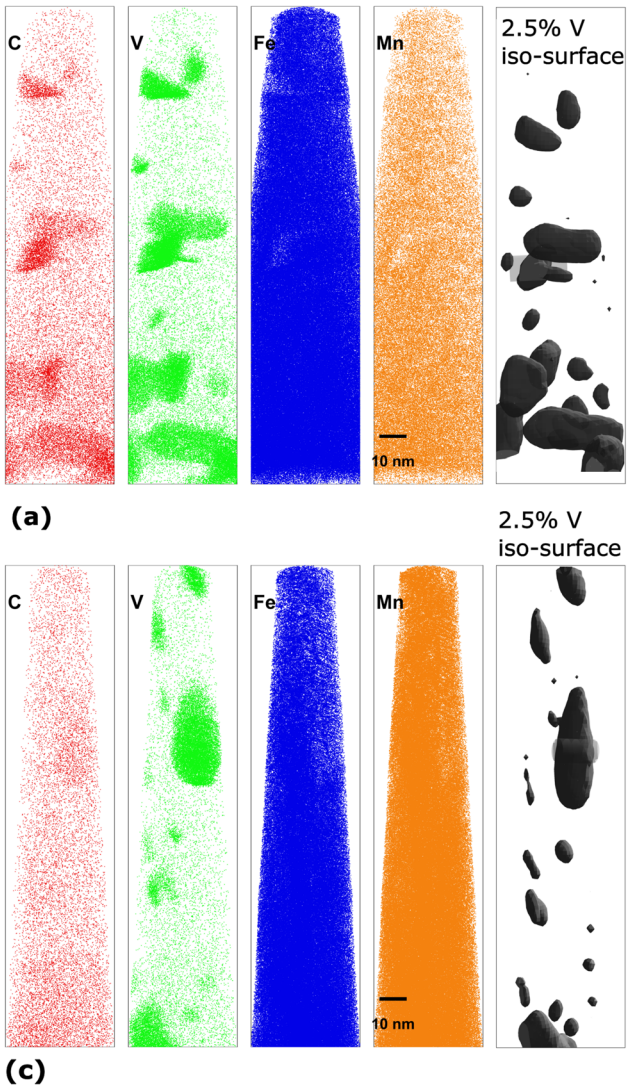

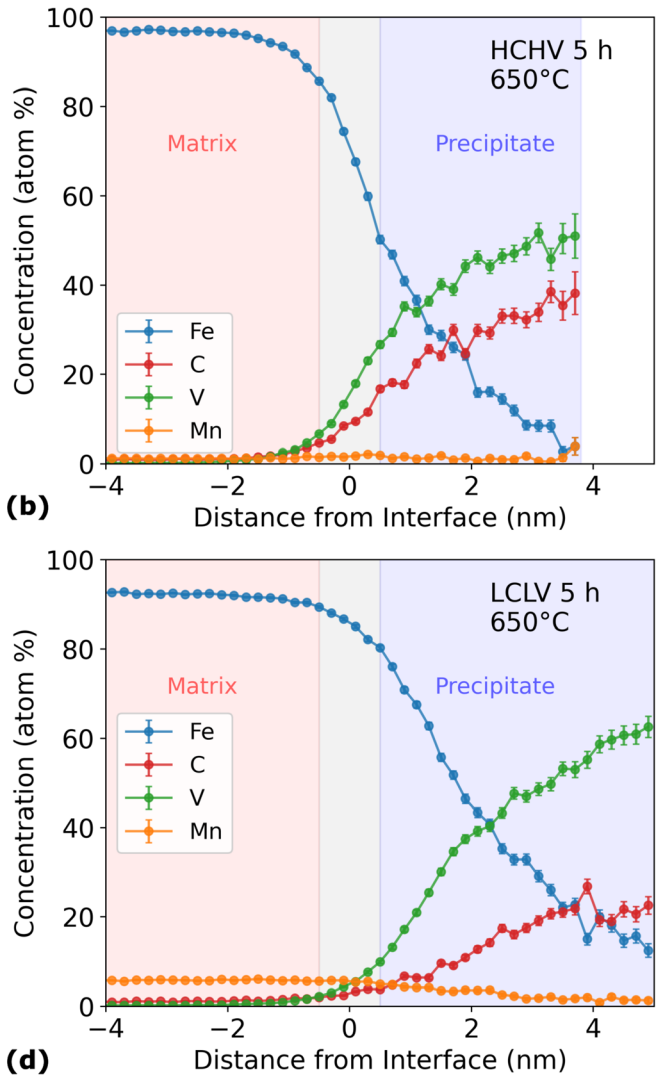

Fig. 3—3D reconstructions of the APT data for (*a*) the HCHV alloy samples and (*c*) the LCLV alloy sample after 5 h aging at 650 °C representing the C, V, Fe and Mn elements. (*b*) and (*d*) Corresponding 2.5 pct V iso-surface from a proxigram analysis for the HCHV and LCLV alloy samples, respectively.

Table II. Measured Compositions of the Main Elements Obtained by APT in the Matrix and Precipitates

	C (At Pct)	V (At Pct)	Fe (At Pct)	Mn (At Pct)
LCLV—Matrix	1.0	0.2	92.6	5.7
LCLV—Precip.	21.7	58.6	17.0	1.6
HCHV—Matrix	0.9	0.2	96.7	1.2
HCHV—Precip.	35.3	49.1	7.4	1.5

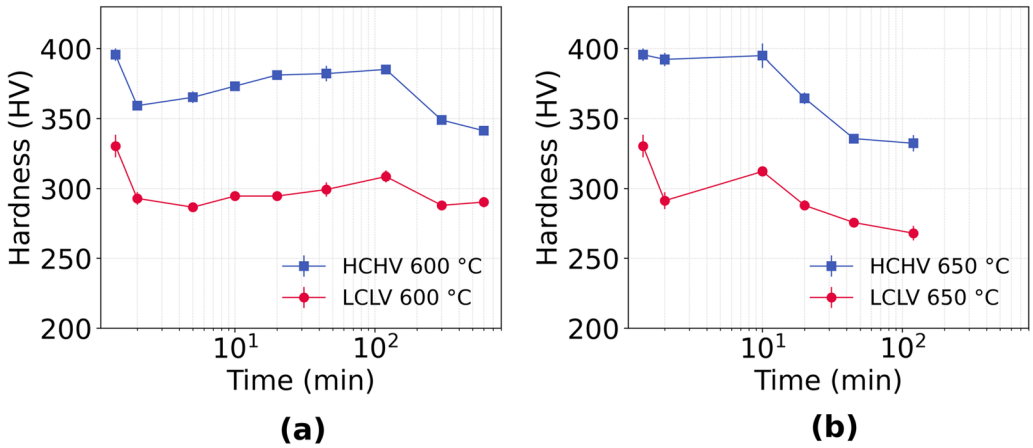

Fig. 4—Vickers hardness as a function of the aging time for the studied HCHV and LCLV alloys at aging temperatures of (*a*) 600 °C and (*b*) 650 °C.

evidence for the role of precipitation strengthening. For longer aging times (10 hours at 600 °C and 2 hours at 650 °C), the observed decrease in hardness is consistent with VC precipitate coarsening, which reduces the precipitation strengthening contribution.

C. *Precipitation Kinetics Studied Using SANS*

1. *Particle size distribution*

To construct a model for the SANS data fitting, we assume, based on the input from STEM and APT (Figures 2 and 3), that the VC precipitates are randomly oriented oblate ellipsoids. The aspect ratio of these oblate ellipsoids is assumed to be $\eta = R_p/R_e = 0.2$, where R_p and R_e are the polar and equatorial radii for the ellipsoid of revolution, respectively. Fitting is performed on the nuclear SANS data to obtain the VC precipitate volume fraction and size distribution. To fit the nuclear SANS data, we use a model with four main elements consisting of two power laws, a log-normal distribution function of oblate elliptical precipitates and a constant background. The two power laws are K_2Q^{-2}andK_4Q^{-4}, where K_2 is assumed to be constant and K_4 is a fit parameter. The SANS from the dislocations is described by the Q^{-2} term and that from (S)GBs is described by the Q^{-4} term.[43–46] A constant background C originates from incoherent scattering. The scattering in the high-Q region (0.02 to 0.1 Å^{-1}) is dominated by the nanoscale VC precipitates. The SANS model for nuclear scattering with elliptical precipitates corresponds to:

$$I(Q)_{nuc} = K_2Q^{-2} + K_4Q^{-4} + (\Delta\rho)^2 \int_0^\infty D_N(R)V^2(R)P(Q,\varphi)dr + C \quad [2]$$

where $\Delta\rho^2$ is the nuclear contrast, $V(R)$ is the volume of the elliptical precipitate and R is the precipitate spatial coordinate. The scattering factor has been modeled as an ellipsoid, which corresponds to $P(Q, \varphi) = |F(Q, \varphi)|^2$ with a form factor $F(Q,r) = 3[\sin(Qr)–(Qr)\cos(Qr)]/(Qr)^3$,[47] where $r(\varphi)$ is given by

$$r(\varphi) = \left[R_e^2 \sin^2\varphi + R_p^2 \cos^2\varphi\right]^{1/2} \quad [3]$$

where φ is the angle between the rotation axis of the ellipsoid of revolution and the scattering vector Q. The orientation of the rotation axis of the ellipsoids is assumed to be randomly distributed and the scattering form factor is averaged accordingly. For the ellipsoids, an equivalent radius (assuming a sphere of equal volume) can be introduced, which corresponds to $R_{eq} = (R_pR_e^2)^{1/3}$. Polydispersity with a log-normal size distribution $D_N(r) = (N_p/[(2\pi)^{1/2}r\sigma])\exp(-[\ln(r)-\ln(r^m)]^2/[2\sigma^2])$ is assumed, where N_p is the number density of precipitates, r_m is the median equivalent radius of the precipitates, and σ is the relative width of the size distribution. The mean inter-precipitate spacing d can be estimated using the number density N_p obtained from:

$$d = \left(N_p\right)^{-\frac{1}{3}} \quad [4]$$

Figure 5 shows the nuclear and magnetic SANS from the HCHV and LCLV alloys, isothermally aged at 650 °C for aging times up to 600 minutes. Figure 5(a) shows the nuclear SANS curves for the HCHV alloy for different aging times. The SANS pattern from the quenched sample (represented by 0 in the figure) shows a fundamentally different scattering behavior than the SANS patterns from the aged samples. A low SANS intensity in the Q range of 0.04 to 0.1 Å^{-1} indicates that no significant VC precipitation has taken place during quenching from the austenitization temperature. In the low-Q region, a strong scattering is observed that is expected to arise from a high density of dislocations and interfaces (such as (S)GBs and nanoscale martensitic lath walls), which are inherent to the martensitic microstructure.

The evolution in the nuclear SANS curves with the isothermal aging time at 650 °C for the HCHV alloy can be observed in Figure 5(a). In the low-Q region (< 0.02 Å^{-1}), a substantial drop in the scattered intensity is observed after just 2 minutes of aging. The intensity only marginally drops for longer aging times (up to 20 minutes), suggesting that the annihilation of a large fraction of the dislocations occurred within the first 2 minutes of aging at 650 °C. In the high-Q region ($>$ 0.02 Å^{-1}), we observe an increase in the scattered intensity just after 2 minutes of aging at 650 °C, indicating a fast nucleation process. A continuous increase in the scattered intensity with aging time is observed, indicating a continuous increase in the VC precipitate phase fraction.

Figure 5(c) shows the nuclear SANS from the LCLV alloy aged for aging times up to 600 minutes at 650 °C. Similar to the HCHV alloy, the SANS pattern from the quenched sample behaves fundamentally differently compared to the SANS patterns from the isothermally aged samples. The decrease in intensity for the LCLV alloy in the low-Q region with increasing aging time is comparable to the results for the HCHV alloy, indicating a similar dislocation annihilation kinetics in both steels. The high-Q SANS signal also increases with aging time, but the increase is less pronounced than that observed for the HCHV alloy [Figure 5(a)]. This indicates a lower VC precipitate volume fraction in the LCLV alloy than in the HCHV alloy, consistent with the equilibrium calculations performed in Thermo-Calc (Figure S2).

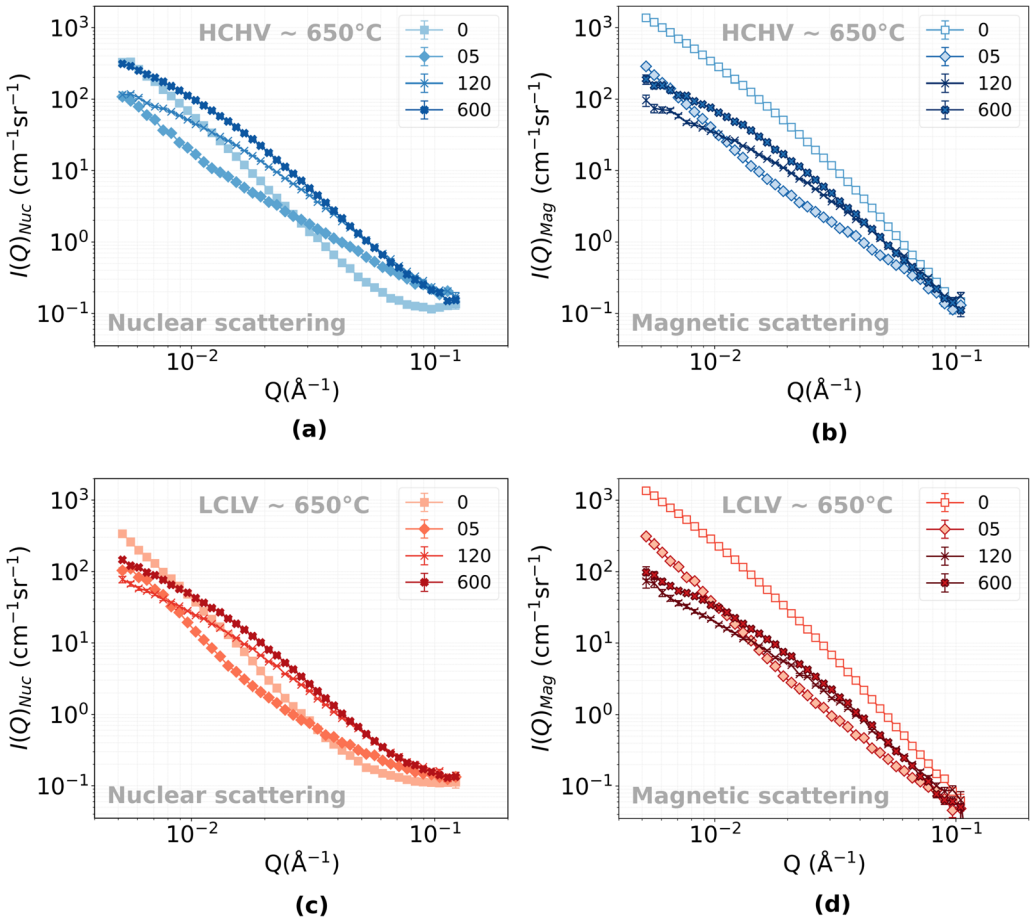

Fig. 5—(*a*) and (*c*) Nuclear and (*b*) and (*d*) magnetic differential scattering cross sections for the HCHV and LCLV alloys as a function of Q measured at room temperature for random VC precipitation during aging at 650 °C for aging times up to 600 min (0 corresponds to the quenched state).

Figures 5(b) and (d) show the magnetic SANS from the HCHV and LCLV alloys, isothermally aged at 650 °C for aging times up to 600 minutes, respectively. The origin of the magnetic SANS is the contrast in magnetization between the ferromagnetic BCC Fe matrix and (1) the paramagnetic VC precipitate, (2) interfaces, and (3) dislocations. The martensitic microstructure contains a high density of interfaces and dislocations, which explains the strong magnetic SANS from the quenched samples. The magnetic SANS in the high-Q region is seen to increase with aging, indicating the formation of nanoscale VC precipitates. However, the scattered intensity from the VC precipitates is weaker for the magnetic SANS than for the nuclear SANS for both the HCHV and LCLV alloys. Therefore, we use the data from nuclear SANS to study the VC precipitation kinetics.

2. *Precipitation kinetics*

To study the VC precipitation kinetics in the LCLV and HCHV alloys, the nuclear SANS data are transformed into the Kratky plots shown in Figure 6. Kratky plotting is a model-free method, which can be used to extract the precipitate volume fraction and average size.[48] To generate a Kratky plot, $I(Q) \times Q^2$ is plotted against Q after subtracting the background. Integrating the area under the Kratky plot provides the invariant Q_0[48,49]:

$$Q_0 = \int_0^\infty I(Q) \times Q^2 dQ = 2\pi^2 \Delta\rho^2 f_v (1 - f_v) \qquad [5]$$

where $\Delta\rho^2$ is the nuclear SANS contrast and f_v is the volume fraction of the VC precipitates. Determination of the invariant Q_0 thereby provides a model independent estimate of the precipitate volume fraction f_v. For both steels, the area under the Kratky plots in Figure 6 increases with aging at 650 °C, indicating an increase in the VC precipitate volume fraction. Moreover, the maximum of the curve shifts to lower Q values with aging, indicating a growth of the VC precipitates.

The model Eq. [2] that describes the nuclear SANS from the studied samples is fitted to the experimental SANS data. Figure 7 shows the evolution of fit parameter K_4 with aging time for both alloys aged at 600 °C and 650 °C. SANS from interfaces such as (S)GBs, martensite block boundaries, and lath walls is described by a power law contribution $K_4 Q^{-4}$, where K_4 is a scaling factor that reflects the interface density. K_4 is found to decrease with aging time at both temperatures, indicating a decrease in the density of interfaces for increasing aging times. This is expected because martensite (sub)grain structures, blocks, and laths tend to grow and coalesce with aging at elevated temperatures.

The K_4 value for the LCLV and HCHV alloys aged for 2 minutes at 600 °C is higher than those obtained at 650 °C. In addition, the decrease in K_4 with aging time is slower at 600 °C than at 650 °C because the recrystallization kinetics is expected to be slower at lower aging temperatures. As martensitic interfaces act as potential nucleation sites for the formation of nanoscale precipitates, it is expected that the precipitate nucleation rate is higher at the early aging stages (≤ 5 minutes) and decreases as the aging proceeds. It is also expected that the nucleation rate reduces faster at 650 °C than at 600 °C.

Figure 8 shows the evolution of the log-normal volume size distribution $D_V = (4/3)\pi R_{eq}^3 D_N$ with aging time for the elliptical precipitates in the HCHV and LCLV alloys aged at 650 °C. The particle size distributions are obtained by fitting the nuclear SANS component to the log-normal size distribution function D_N. The area under each curve indicates the precipitate volume fraction, whereas the maximum of each curve represents the median equivalent radius of the VC precipitates. For both alloys, the maximum of the particle size distribution shifts to larger radii with aging, indicating precipitate growth. The area under the curve is observed to increase with aging for both alloys, indicating a continuous increase in the precipitate volume fraction during aging, as also evidenced by the Kratky plots (Figure 6).

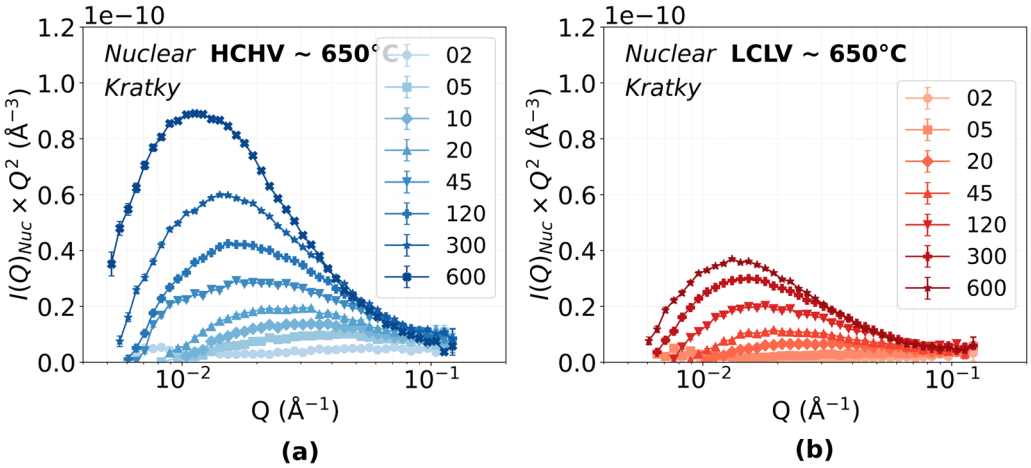

Fig. 6—Kratky plots for the nuclear SANS from VC precipitates in the (*a*) HCHV and (*b*) LCLV alloys for different aging times at an aging temperature of 650 °C.

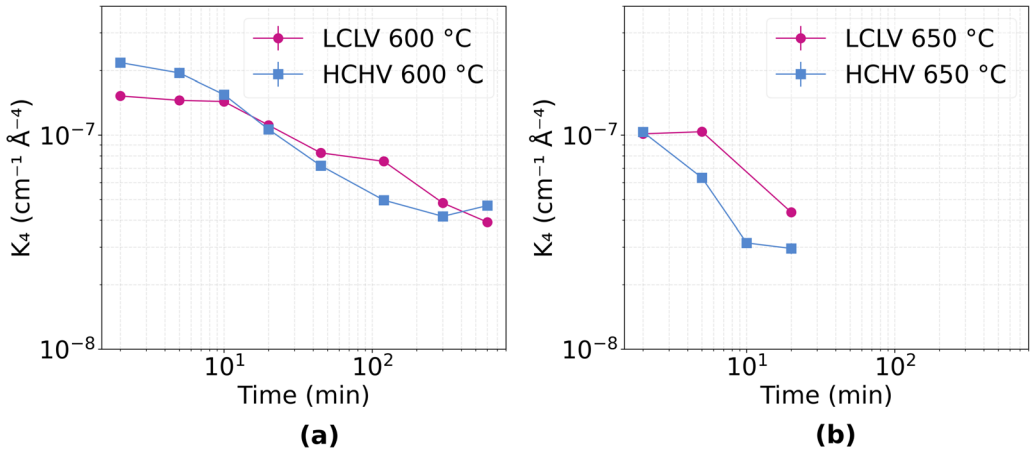

Fig. 7—K_4 fit parameter for the nuclear SANS from the LCLV and HCHV alloys as a function of aging time for aging at temperatures of (*a*) 600 °C and (*b*) 650 °C.

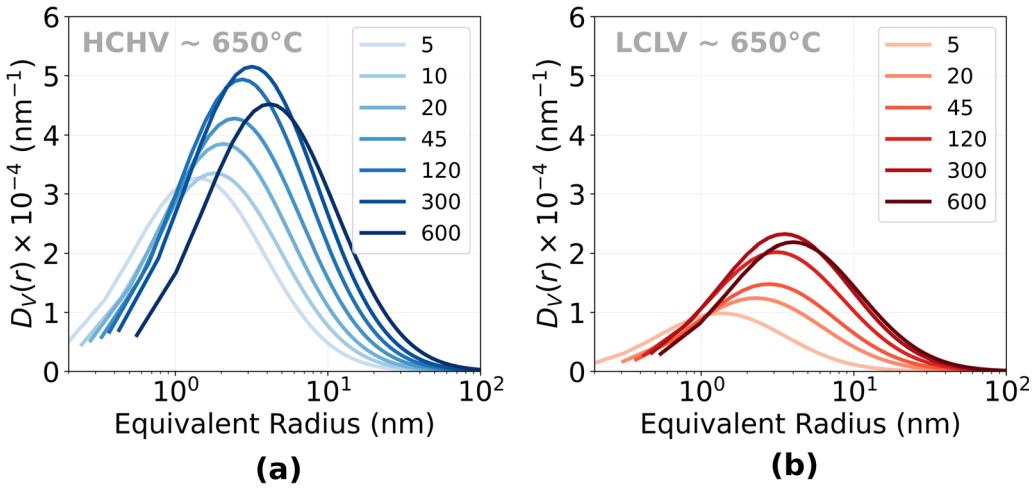

Fig. 8—VC precipitate volume size distribution D_V as a function of the equivalent precipitate radius R_{eq} for different aging times at 650 °C for the (*a*) HCHV alloy and the (*b*) LCLV alloy, with a shared y-axis for both plots.

In Figure 9(a), the VC precipitate volume fraction as a function of aging time at 650 °C is presented for both the HCHV and LCLV alloys. The VC volume fractions increase with aging in both alloys, but after 600 minutes of aging, they do not yet reach the corresponding equilibrium values predicted by Thermo-Calc. Over the full course of aging, a higher volume fraction is observed in the HCHV alloy than in the LCLV alloy. A sharp increase in the volume fraction is observed during the first 5 minutes of aging at 650 °C. A rapid initial precipitation kinetics is observed for the HCHV alloy. This can be explained by the co-existence of two phenomena. First, the martensite phase contains an extremely high density of potential nucleation sites, including dislocations and interfaces such as (S)GBs, block boundaries, and lath boundaries. This abundance of potential nucleation sites results in burst-like nucleation. Second, carbon and vanadium diffuse rapidly along these interfaces and dislocations, which act as fast diffusion pathways.[18] The combination of these two phenomena provides favorable conditions for rapid initial precipitation kinetics. In both the HCHV and LCLV alloys, the VC volume fraction increases continuously with aging, reaching maximum values at the maximum aging time of 600 minutes at 650 °C of 0.77 and 0.36 pct, respectively. The fraction transformed (in pct) of the VC precipitation is estimated by $100 \times (f_{v,600}/f_{v,eqb})$, where $f_{v,eqb}$ is the equilibrium VC precipitate volume fraction and $f_{v,600}$ is the volume fraction after 600 minutes of aging at 650 °C. This results in transformed fractions of 71 pct for the HCHV alloy and 66 pct for the LCLV alloy.

In Figure 9(b), the evolution in equivalent radius of VC precipitates with aging at 650 °C is reported for the HCHV and LCLV alloys. Continuous precipitate growth is observed during aging for both steels. After 5 minutes of aging at 650 °C, VC precipitates with comparable median equivalent radii of 3.8 and 3.4 nm are detected in the HCHV and LCLV alloys, respectively. This indicates that rapid growth occurs for short aging times (< 5 minutes), which can be explained by fast carbon and vanadium diffusion along dislocations

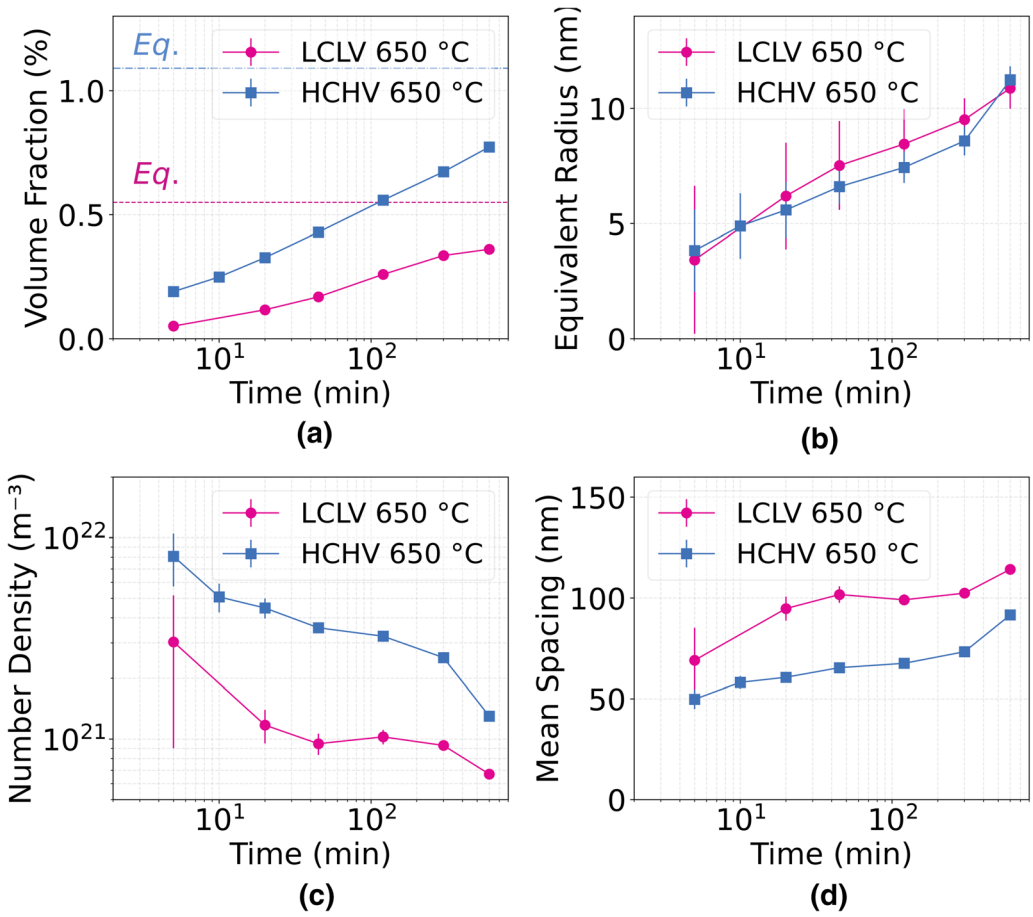

Fig. 9—Statistical data of random VC precipitates derived from nuclear SANS fitting results for the HCHV and LCLV alloys as a function of aging time at 650 °C: (*a*) volume fraction, (*b*) equivalent radius, (*c*) number density and (*d*) mean spacing of the precipitates.

and interfaces. Additionally, a weak sensitivity of the precipitate size on the carbon and vanadium concentrations is identified. After 600 minutes of aging, comparable precipitate sizes are observed in both alloys, with a median equivalent radius of 11.2 nm in the HCHV alloy and 10.9 nm in the LCLV alloy, in close agreement with the STEM measurements [Figures 2(i) and (j)].

The evolution of the VC precipitate number density with aging time at 650 °C is reported in Figure 9(c). Over the full course of aging, the highest precipitate number density is observed during the early aging stages (≤ 5 minutes) for both alloys. After 600 minutes of aging, the precipitate number density decreases by a factor 6.5 for the HCHV alloy and a factor of 5 for the LCLV alloy. The VC precipitate number density in the HCHV alloy is consistently higher than that in the LCLV alloy.

From these observations, we deduce that applying a fast heating rate (50 °C/s) to reach the aging temperatures of 600 °C and 650 °C does indeed preserve the high density of potential nucleation sites in the initial martensitic microstructures. This high density of potential nucleation sites stimulates VC nucleation during the early aging stages (≤ 5 minutes). However, the potential nucleation sites rapidly decrease for longer aging times, as indicated by the reduction in the power law pre-factor K_4 and precipitate number density [Figures 7 and 9(c)]. The continuous decrease in the VC precipitate number density indicates that coarsening of precipitates already starts well before the VC precipitation kinetics is completed (the precipitate volume fractions remain well below the equilibrium values for the studied aging periods). Figure 9(d) shows the average precipitate spacing estimated using Eq. [4]. The continuous increase in the mean precipitate spacing reflects the effect of precipitate coarsening. The corresponding statistical data of random VC precipitation at 600 °C are shown in Figure S5.

IV. DISCUSSION

A. *Random Precipitation Kinetics*

The kinetics of VC formation through RP is controlled by nucleation, growth and coarsening. The early aging period is dominated by a rapid VC nucleation process, as indicated by the high initial precipitate number density in Figure 9(c). To evaluate the precipitate growth kinetics, the model developed by Offerman and coworkers[50] is used in which the growth is controlled by the volume diffusion of solutes (in this case vanadium). The growth model is illustrated in

Figure S6, where a linear concentration profile of vanadium atoms away from the precipitate-matrix interface is assumed. The calculated diffusion length is L (see supplementary information section 6) and the precipitate equivalent radius, R_{eq}, is experimentally obtained by SANS. Next, $2(R_{eq} + L)$ is calculated and compared against the experimental mean inter-precipitate spacing, d. Two adjacent precipitates have overlapping diffusion fields when $2(R_{eq} + L) > d$. This phenomenon is known as soft impingement. During soft impingement, adjacent precipitates compete for solute atoms (C and V) during their growth.

At holding temperature of 650 °C, soft impingement is estimated to begin after an aging period of 6 minutes for the LCLV alloy and in less than 5 minutes for the HCHV alloy, indicating that elevated vanadium and carbon concentrations in the HCHV alloy accelerate the onset of soft impingement (see Figure 10). This earlier onset means that precipitates in the HCHV alloy begin to compete for solute atoms sooner, limiting their individual growth rates at an earlier aging stage. Consequently, precipitates in the LCLV alloy can grow unimpeded for a longer period before diffusion fields overlap, resulting in the larger precipitate sizes in the LCLV alloy [Figure 9(b)].

VC precipitate coarsening is a process in which larger precipitates grow at the expense of smaller ones, reducing the total precipitate–matrix interfacial area and thereby lowering the overall system energy. The continuous decrease in precipitate number density observed during early aging in both the LCLV and HCHV alloys indicates that coarsening is already active from the early stages of the aging process, occurring concurrently with ongoing precipitation. To describe the coarsening kinetics, a generalized power law relationship is adopted[51,52]

$$R_m = (Kt)^n \qquad [6]$$

where R_m is the mean equivalent precipitate radius, t is the aging time, and K is the temperature-dependent coarsening rate constant. While the classical LSW theory predicts an exponent of $n = 1/3$ for bulk diffusion-controlled coarsening, the exponent n is here treated as a free fitting parameter, allowing the dominant mass transport mechanism to be inferred from the experimental data. Values of n deviating from 1/3 may instead reflect the dominance of alternative diffusion mechanisms, such as interface diffusion ($n = 1/4$) or pipe diffusion along dislocations ($n = 1/5$).[53] It should be noted, however, that the LSW framework strictly assumes a constant precipitate volume fraction, a condition that is not fully met in the present study where the volume fraction continues to evolve during aging. The LSW framework is therefore applied here in an approximate capacity rather than as a rigorous mechanistic model. Such use of LSW-based power law fitting is commonly adopted in the literature for systems where precipitation and coarsening overlap temporally, with the understanding that the extracted exponents provide useful qualitative insight into the rate-controlling diffusion mechanism.[54] The rate constant depends on the solute solubility and diffusion kinetics according to

$$K \propto \frac{\gamma C_\infty}{T} exp\left(-\frac{Q}{k_B T}\right) \qquad [7]$$

where γ is the interfacial energy, C_∞ is the solubility limit of V in the BCC Fe matrix, Q is the activation energy for bulk V diffusion, T is the absolute temperature, and k_B is the Boltzmann's constant.

Figure 11 shows power law fits for the time-dependent VC precipitate radius $R_m(t)$ obtained from SANS. The fitted exponents are $n = 0.20 \pm 0.02$ for HCHV and $n = 0.15 \pm 0.01$ for LCLV. The observed exponents in the present study fall closest to the $n = 1/5$ regime, suggesting pipe diffusion as the more likely dominant mechanism, over interfacial diffusion. This interpretation is physically consistent with the martensitic microstructure of both alloys, which is characterized by a high dislocation density that can provide preferential diffusion pathways and promote faster solute transport compared to bulk diffusion.

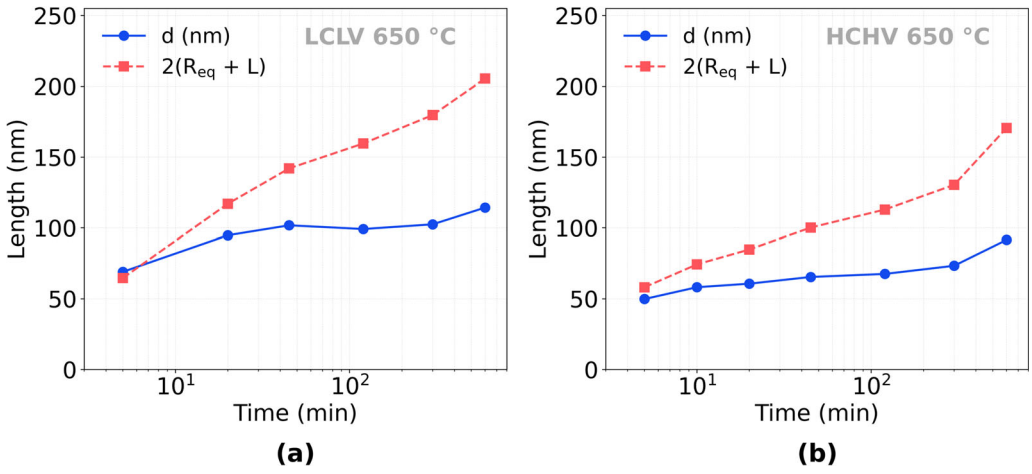

Fig. 10—Calculated linear diffusion length of vanadium, L, for the (*a*) LCLV alloy and the (*b*) HCHV alloy for aging at 650 °C. d: inter-precipitate spacing, R_{eq}: equivalent precipitate radius.

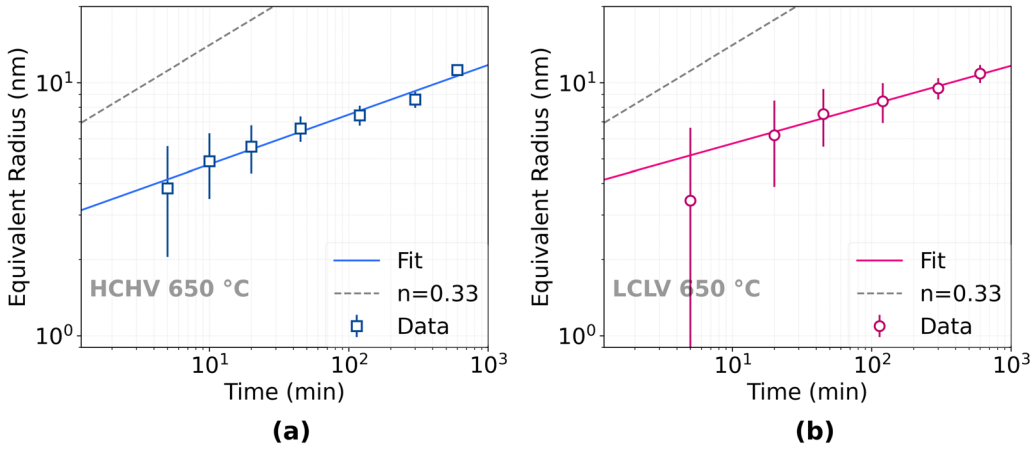

Fig. 11—LSW model fit to the experimental SANS data. The blue open squares represent the VC radius in the HCHV alloy (*a*), and the pink open circles represent the VC radius in the LCLV alloy (*b*). The fitted curves are represented by the solid lines. The dashed curve represents the time dependence for an exponent of $n = 0.33$ in Eq. [6].

The coarsening analysis identifies pipe diffusion along dislocations as the dominant transport mechanism, and TEM reveals oblate ellipsoidal VC precipitate morphologies. Based on these observations, it is reasonable to propose that solutes first migrate from the matrix to nearby dislocations, which then serve as preferential diffusion pathways within an interconnected dislocation interface network, ultimately delivering solute to the interfaces where VC precipitates nucleate and grow.

B. *Time-Dependent VC Precipitation Strengthening*

To estimate the increase in strength of the steels by VC precipitation we use the Ashby–Orowan strengthening model.[9] This model relates the increase in strength to the volume fraction and radius of the precipitates:

$$\Delta\sigma = \frac{0.538Gb\sqrt{f_v}}{2r}\ln\left(\frac{r}{b}\right) \quad [8]$$

where $\Delta\sigma$ is the increase in strength resulting from the precipitation hardening, G is the shear modulus of the matrix, b is the Burgers vector, f_v is the volume fraction of the precipitates, and r is the average (equivalent) radius of the precipitates. For $G = 81600$ MPa and $b = a\sqrt{3}/2$, with $a = 2.86$ Å being the lattice parameter of the BCC Fe-based matrix, it becomes possible to calculate the increase in strength by the VC precipitate formation. Introducing scaled variables $x = r/b$, and $A = 0.538G\sqrt{f_v}/2$ to the Ashby-Orowan equation transforms it into $\Delta\sigma = A(\ln x)/x$. Evaluating $d\Delta\sigma/dx = 0$ gives the precipitate radius which results in the maximum strengthening. This is visualized in contour plots for the HCHV and LCLV alloys, where the maximum strengthening can be found in the upper left regions of Figures 12(a) and (b) for aging temperatures of 600 °C and 650 °C, respectively. Using the SANS results, peak strength increments of 223 MPa for the HCHV alloy and 143 MPa for the LCLV alloy are estimated for the aging temperature of 650 °C.

To distinguish between shearing and bypassing as the dominant precipitation strengthening mechanisms, a critical precipitate radius of $R_c = 2$ nm is used as a representative threshold for VC precipitates in ferritic steels.[55] This threshold reflects the size-dependent nature of dislocation–precipitate interactions, where small, coherent precipitates tend to be sheared by mobile dislocations, while precipitates growing beyond R_c generally become semi-coherent or incoherent with the ferritic matrix, favoring a transition toward the Orowan bypassing mechanism. Based on this, the active strengthening mechanism is considered to be (a) dislocation shearing ($R < R_c$) or (b) Orowan bypassing ($R > R_c$), where R is the median equivalent radius of the VC precipitates determined by SANS.

In both LCLV and HCHV steels, the measured VC precipitate radii exceed R_c at both aging temperatures (600 °C and 650 °C) from the earliest aging time of 5 minutes, with median radii of 3.4 ± 3.2 and 3.8 ± 1.8 nm, respectively. This suggests that Orowan bypassing is likely the dominant strengthening mechanism throughout the aging sequence in both alloys. The maximum contribution to yield strength from VC precipitation appears to be reached after approximately 120 and 300 minutes of aging in the HCHV and LCLV steels, respectively [Figure 13(d)], after which continued coarsening is expected to gradually reduce the VC strengthening. Consequently, the application of the Ashby–Orowan equation to quantify VC precipitation strengthening in this work is physically justified by the precipitate size criterion, consistent with its use in a previous studies[56,57] for nanoprecipitate strengthening quantification.

C. *Nuclear to Magnetic SANS Ratio Evolution*

The A-factor,[10] defined as the ratio of the nuclear to magnetic SANS intensity, exhibits a clear evolution with aging time at both 600 °C and 650 °C in both the HCHV and LCLV alloys (Figure 14). This time-dependent evolution indicates a compositional change within

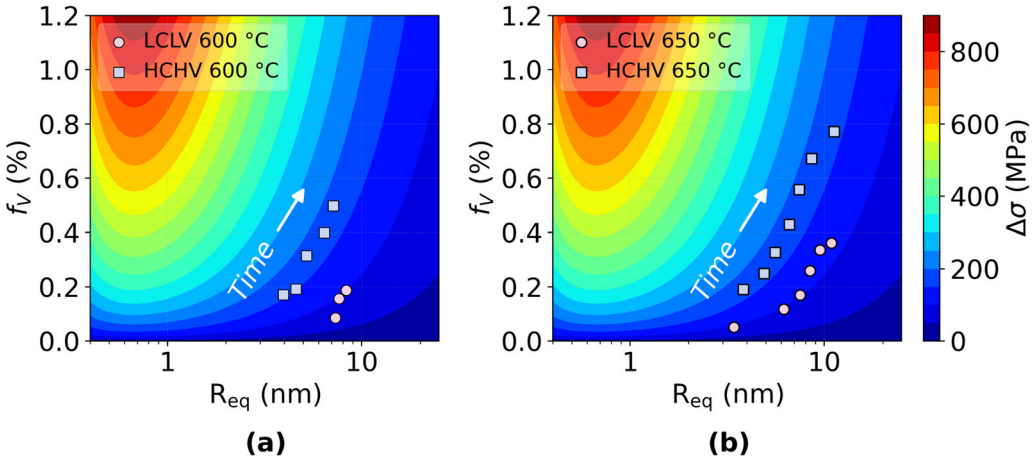

Fig. 12—Contour plots of the Ashby-Orowan equation illustrating the strength increment by VC precipitation as a function of the precipitate radius and volume fraction in the LCLV and HCHV alloys at aging temperatures of (*a*) 600 °C and (*b*) 650 °C.

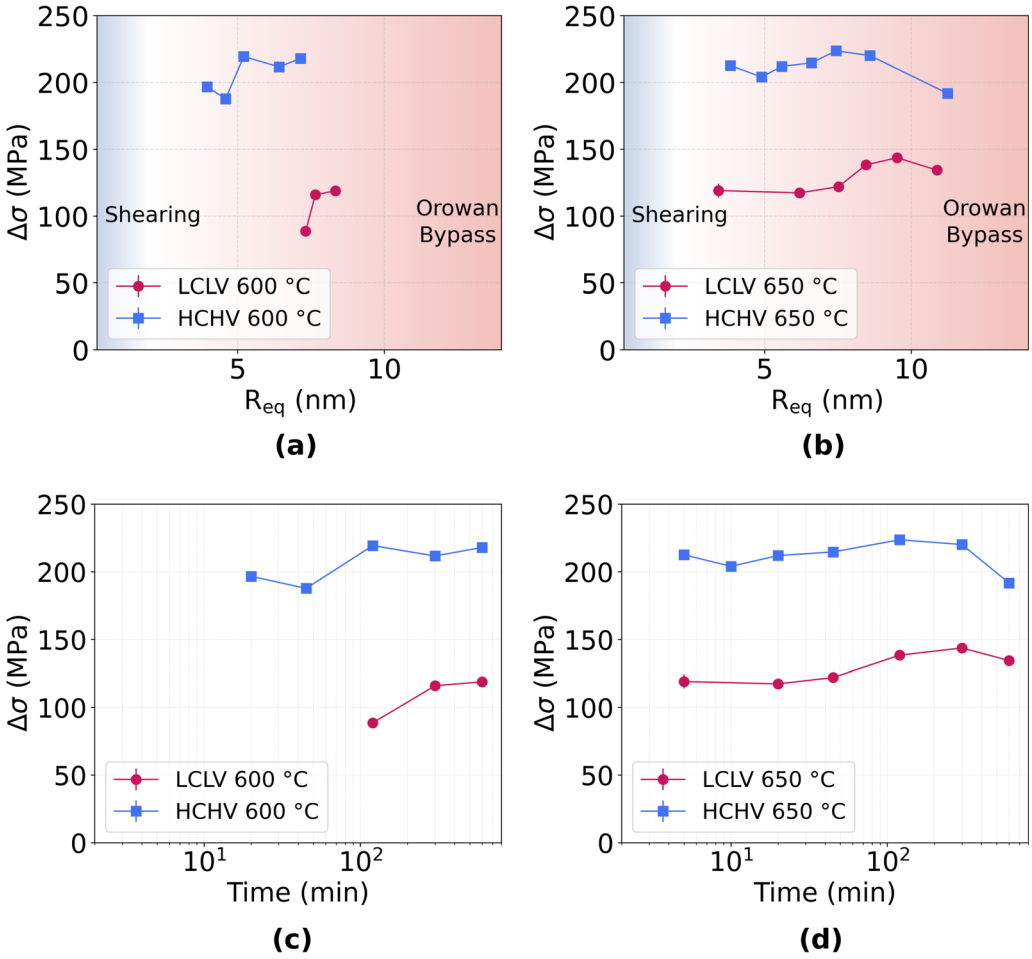

Fig. 13—Strength enhancement *vs* VC precipitate size for the LCLV and HCHV alloys aged at (*a*) 600 °C and (*b*) 650 °C. The blue and red regions show the size ranges where precipitate shearing and Orowan bypassing are the dominant strengthening mechanisms, respectively. (*c*) and (*d*) Strength enhancement *vs* aging time for the LCLV and HCHV alloys aged at 600 °C and 650 °C, respectively.

the precipitates as aging progresses. The low A-factor values observed at early aging times are consistent with iron enrichment in the precipitates shortly after quenching, with the precipitates becoming progressively depleted of Fe as aging continues. At longer aging times, the A-factor trends toward the equilibrium value, though a deviation from the reference value persists across all conditions. The equilibrium A-factor value

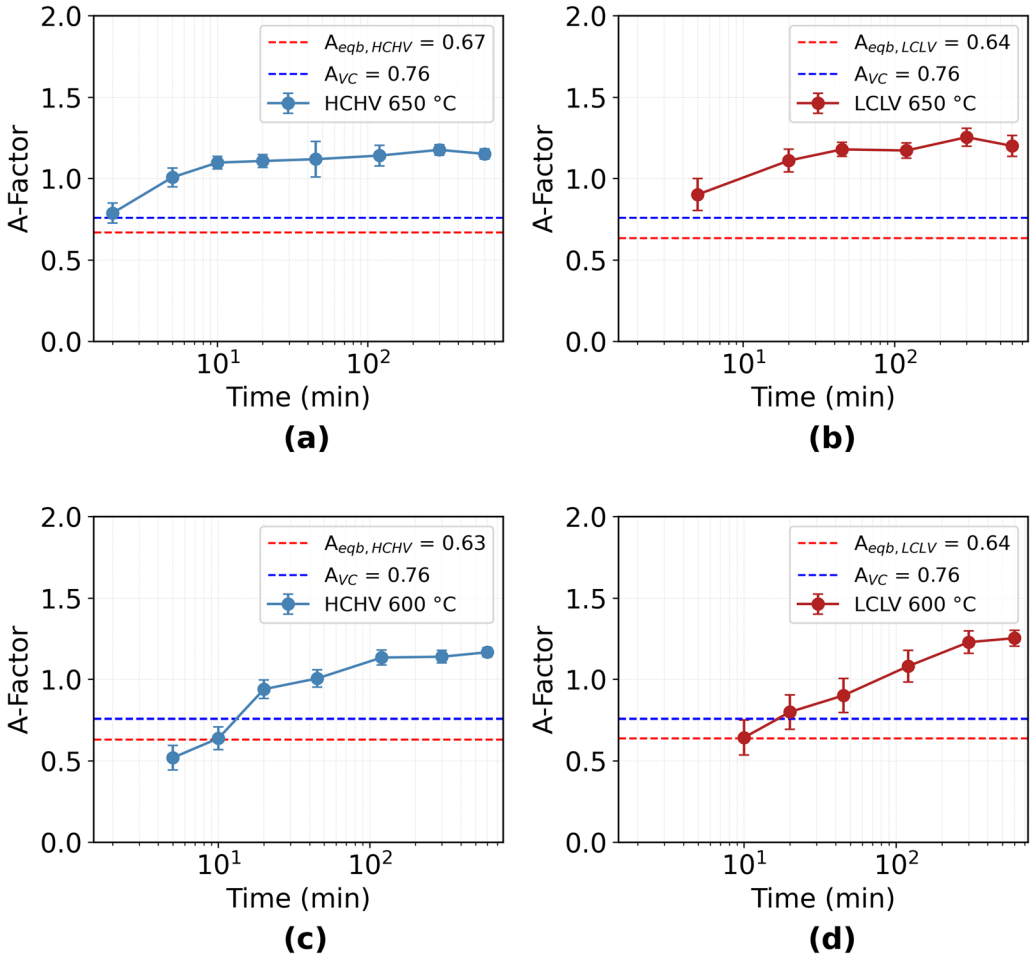

Fig. 14—A-factor as a function of aging time for (*a*) HCHV aged at 650 °C, (*b*) LCLV aged at 650 °C, (*c*) HCHV aged at 600 °C, and (*d*) LCLV aged at 600 °C. The A-factor is calculated as the ratio of the nuclear to magnetic SANS intensity, averaged over the Q range 0.03 to 0.05 $Å^{-1}$. The red dashed line indicates the calculated A-factor value determined from assuming equilibrium precipitate compositions, and the blue dashed line indicates the theoretical A-factor for a stoichiometric V_1C_1 precipitate. Error bars represent the standard error of the mean.

used as reference was calculated using the equilibrium precipitate composition predicted by Thermo-Calc (TCFE14). This discrepancy may arise from uncertainties in power law corrections for the nuclear and magnetic SANS signals. While the background contributions to nuclear SANS from dislocations and interfaces are relatively well documented in the literature and can be reasonably accounted for, accurately subtracting the background from the magnetic SANS component is considerably more challenging, introducing a systematic uncertainty in the A-factor calculation.

Interestingly, APT measurements reveal a vanadium enrichment in the precipitates, which is broadly consistent with the elevated A-factor values observed particularly at longer aging times, as a higher vanadium content in the VC precipitates would result in an increase of the nuclear-to-magnetic scattering ratio. However, deconvoluting the contribution of vanadium enrichment from the systematic errors introduced by inaccuracies in magnetic power law corrections is challenging with the present room-temperature SANS data.

V. CONCLUSIONS

We have performed room-temperature small-angle neutron scattering (SANS) measurements on two differently composed vanadium micro-alloyed nanosteels to study the vanadium carbide (VC) random precipitation (RP) kinetics at two different aging temperatures of 600 °C and 650 °C. The effect of varying V and C concentrations was studied. In both alloys, the evolution of the VC precipitate size distribution was monitored. Complementary atom probe tomography (APT) and scanning transmission electron microscopy (STEM) experiments were performed for investigating VC precipitate shape, morphology and composition. The mechanical behavior of both steels was evaluated by hardness tests as a function of aging time and temperature. The main conclusions derived from this study are as follows:

1. Random VC precipitation occurs mainly at martensitic interfaces and dislocations, resulting in oblate ellipsoidal VC precipitates.
2. Random VC precipitation results in burst nucleation and rapid precipitate growth due to the

presence of a high density of favorable nucleation sites and enhanced solute diffusion along dislocations and martensitic interfaces.
3. An accelerated VC precipitate coarsening is observed that reduces the total precipitate-matrix interfacial energy. The dominant mechanism controlling precipitate coarsening is pipe diffusion along dislocations.
4. The increase in strength by VC precipitate formation is estimated using the Ashby-Orowan strengthening model. It is found that at 650 °C, the VC strengthening peaks at an aging time of 120 minutes for the HCHV steel and at 300 minutes for the LCLV steel.
5. The time-dependent evolution of the A-factor indicates a progressive compositional change in the VC precipitates during aging.

ACKNOWLEDGMENTS

This research was carried out under project number 19470-NWO/N21014-M2i in the framework of the Partnership Program of the Materials innovation institute M2i (www.m2i.nl) and the Technology Foundation TTW (www.stw.nl), which is part of the Netherlands Organization for Scientific Research (www.nwo.nl). Tata Steel (IJmuiden, The Netherlands) is acknowledged for providing the material for this study. The atom probe work was carried out at the Hultgren Laboratory, KTH. Funding for the atom probe instrument was provided by Hugo Carlsson's Research Foundation, Jernkontoret, KTH Research Infrastructure, and the KTH Department of Materials Science and Engineering. The authors would like to acknowledge the use of the LARMOR instrument at ISIS, STFC, UK. The help of the support staff from ISIS during the neutron experiments is greatly appreciated. The authors thank Nico Geerlofs for his assistance with the heat treatments. The authors would like to thank Arjan Rijkenberg (Tata Steel) for his contributions to alloy design and process development, and Winfried Kranendonk (Tata Steel) and Pina Mecozzi for fruitful discussions.

AUTHOR CONTRIBUTIONS

Zamran Zahoor Khan: Conceptualization, methodology, investigation, formal analysis, visualization, validation, data curation, writing—original draft preparation, writing—review & editing, project administration. Amir Sabet Ghorabaei and Sonia Guehairia: Methodology, investigation, formal analysis, visualization, validation, data curation, writing—original draft preparation, writing—review & editing. Steven R. Parnell: Methodology, validation, supervision, writing—review & editing. Dirk Honecker and Peter Hedström: Methodology, writing—review & editing. Bart J. Kooi: Supervision, resources, funding acquisition, methodology, validation, data curation, writing—review & editing, project administration. Sven Erik Offerman and Niels H. van Dijk: Conceptualization, cupervision, resources, funding acquisition, methodology, validation, data curation, writing—review & editing, project administration.

DATA AVAILABILITY

The data are available from the corresponding author upon reasonable request.

COMPETING INTERESTS

The authors declare that they have no known competing financial interests or personal relationships that could have appeared to influence the work reported in this paper.

OPEN ACCESS

SUPPLEMENTARY INFORMATION

The online version contains supplementary material available at https://doi.org/10.1007/s11661-026-08288-8.

REFERENCES

1. Y. Funakawa, T. Shiozaki, K. Tomita, T. Yamamoto, and E. Maeda: *ISIJ Int.*, 2004, vol. 44, pp. 1945–51.
2. K. Seto, Y. Funakawa, and S. Kanekom: *JFE Technical Report*, 2007, No. 10.
3. D. Raabe, D. Ponge, O. Dmitrieva, and B. Sander: *Scr. Mater.*, 2009, vol. 60, pp. 1141–4.
4. S. Jiang, H. Wang, Y. Wu, X. Liu, H. Chen, M. Yao, B. Gault, D. Ponge, D. Raabe, A. Hirata, M. Chen, Y. Wang, and Z. Lu: *Nature*, 2017, vol. 544, pp. 460–4.

5. D. Raabe, D. Ponge, O. Dmitrieva, and B. Sander: *Adv. Eng. Mater.*, 2009, vol. 11, pp. 547–55.
6. K. Kawajiri, M. Kobayashi, and K. Sakamoto: *J. Clean. Prod.*, 2020, vol. 253, pp. 0959–6526.
7. A. Cui, X. Wang, and Y. Cui: *J. Mater. Sci.: Mater. Theory*, 2024, vol. 8, p. 13.
8. A. Deschamps and C.R. Hutchinson: *Acta Mater.*, 2021, vol. 220, p. 117338.
9. T. Gladman: *Mater. Sci. Technol.*, 1999, vol. 15, pp. 30–6.
10. Z.Z. Khan, S.R. Parnell, S.E. Offerman, D.A. Venero, A.S. Ghorabaei, B.J. Kooi, and N. van Dijk: *J. Mater. Sci.*, 2025, vol. 60, pp. 7002–19.
11. R.W.K. Honeycombe and R.F. Mehl: *Metall. Trans. A*, 1976, vol. A7, pp. 915–36.
12. R. Okamoto and J. Ågren: *Acta Mater.*, 2010, vol. 58, pp. 4791–803.
13. M.-Y. Chen, M. Gouné, M. Militzer, Y. Bréchet, and J.-R. Yang: *Metall. Mater. Trans. A*, 2014, vol. 45A, pp. 5351–61.
14. Y.-J. Zhang, G. Miyamoto, K. Shinbo, T. Furuhara, T. Ohmura, T. Suzuki, and K. Tsuzaki: *Acta Mater.*, 2015, vol. 84, pp. 375–84.
15. H. Dong, H. Chen, B. Zhang, Y. Zhang, Z. Wang, X. Zhou, W. Wang, H. Wang, T. Li, Z. Yang, and S. van der Zwaag: *Acta Mater.*, 2022, vol. 223, p. 117475.
16. C. Ioannidou, A. Navarro-López, R.M. Dalgliesh, A. Rijkenberg, X. Zhang, B. Kooi, N. Geerlofs, C. Pappas, J. Sietsma, A.A. van Well, and S.E. Offerman: *Acta Mater.*, 2021, vol. 220, p. 117317.
17. J. Kučera and K. Stránský: *Mater. Sci. Eng.*, 1982, vol. 52, pp. 1–38.
18. C.E.I.C. Öhlund, J. Weidow, M. Thuvander, and S.E. Offerman: *ISIJ Int.*, 2014, vol. 54, pp. 2890–99.
19. H.K.D.H. Bhadeshia and R.W.K. Honeycombe: *Steels: microstructure and properties*, 3rd ed. Butterworth-Heinemann, 2006, pp. 83–114.
20. M.-Y. Chen, M. Gouné, M. Verdier, Y. Bréchet, and J.-R. Yang: *Acta Mater.*, 2014, vol. 64, pp. 78–92.
21. G. Miyamoto, R. Hori, B. Poorganji, and T. Furuhara: *ISIJ Int.*, 2011, vol. 51, pp. 1733–39.
22. T.N. Baker: *Mater. Sci. Tech.*, 2009, vol. 25, pp. 1083–1107.
23. A. Kurlov: *Inorg. Mater.*, 2019, vol. 55, pp. 223–30.
24. P. Gong, X.G. Liu, A. Rijkenberg, and W.M. Rainforth: *Acta Mater.*, 2018, vol. 161, pp. 374–87.
25. K. Nakamura and M. Yashima: *Mater. Sci. Eng. B*, 2008, vol. 148, pp. 69–72.
26. C. Ioannidou, A. Navarro-López, A. Rijkenberg, R.M. Dalgliesh, S. Koelling, C. Pappas, J. Sietsma, A.A. van Well, and S.E. Offerman: *Acta Mater.*, 2020, vol. 201, pp. 217–30.
27. G. Miyamoto, R. Hori, B. Poorganji, and T. Furuhara: *ISIJ Int.*, 2011, vol. 51(10), pp. 1733–9.
28. G. Spartacus, J. Malaplate, F. De Geuser, I. Mouton, D. Sornin, R. Guillou, and A. Deschamps: *Acta Mater.*, 2024, vol. 280, p. 120328.
29. B. Hammouda: *Probing nanoscale structures – The SANS toolbox*, pp. 86-213.
30. O. Arnold, J.C. Bilheux, J.M. Borreguero, A. Buts, S.I. Campbell, L. Chapon, M. Doucet, N. Draper, R.F. Leal, M.A. Gigg, and V.E. Lynch: *Nucl. Instrum. Methods Phys. Res. A*, 2014, vol. 764, pp. 156–66.
31. M. Doucet et al.: SAS view software: SasView Version 5.0.6. https://doi.org/10.5281/zenodo.7581379.
32. A.S. Ghorabaei and B.J. Kooi: *J. Mater. Res. Technol.*, 2024, vol. 30, pp. 6418–29.
33. P.J. Felfer, T. Alam, S.P. Ringer, and J.M. Cairney: *Microsc. Res. Tech.*, 2012, vol. 75, pp. 484–91.
34. M.K. Miller: *Atom Probe Tomography: Analysis at the Atomic Level*, 1st ed. Springer, US, Boston, 2000.
35. B. Gault, in Atom probe microscopy, *Springer series in materials science*, no. 160 (Springer, New York, 2012).
36. D.N. Seidman: *Annual Rev. Mater. Res.*, 2007, vol. 37, pp. 127–58.
37. T.F. Kelly and D.J. Larson: *Annual Rev Mater. Res.*, 2012, vol. 42, pp. 1–31.
38. L. Yao, J.M. Cairney, C. Zhu, and S.P. Ringer: *Ultramicroscopy*, 2011, vol. 111, pp. 648–51.
39. D. Haley and A. London: Depict, APTTools, 2020. http://apttools.sourceforge.net.
40. O.C. Hellman, J.A. Vandenbroucke, J. Rüsing, D. Isheim, and D.N. Seidman: *Microsc. Microanal.*, 2000, vol. 6, pp. 437–44.
41. L.T. Stephenson, M.P. Moody, P.V. Liddicoat, and S.P. Ringer: *Microsc. Microanal.*, 2007, vol. 13, pp. 448–63.
42. C.E.I.C. Öhlund, J. Weidow, M. Thuvander, and S.E. Offerman: *ISIJ Int.*, 2015, vol. 55, pp. 884–93.
43. G.G. Long and L.E. Levine: *Acta Cryst.*, 2005, vol. A61, pp. 557–67.
44. G.G. Long, L.E. Levine, and R. Thomson: *Acta Cryst.*, 1995, vol. A55, pp. 433–47.
45. B.J. Heuser: *J. Appl. Cryst.*, 1994, vol. 27, pp. 1020–29.
46. H.H. Atkinson and P.B. Hirsch: *Philos. Mag.*, 1958, vol. 3, pp. 213–28.
47. B.T.M. Willis and C.J. Carlile: *Experimental neutron scattering*, Oxford University Press, Oxford, 2009.
48. A. Deschamps and F. De Geuser: *J. Appl. Cryst.*, 2011, vol. 44, pp. 343–52.
49. T. Claudio, N. Stein, D.G. Stroppa, B. Klobes, M.M. Koza, P. Kudejova, N. Petermann, H. Wiggers, G. Schierning, and R.P. Hermann: *Phys. Chem. Chem. Phys.*, 2014, vol. 16(47), pp. 25701–9.
50. S.E. Offerman, N.H. Van Dijk, J. Sietsma, E.M. Lauridsen, L. Margulies, S. Grigull, H.F. Poulsen, and S. Van der Zwaag: *Acta Mater.*, 2004, vol. 52, pp. 4757–66.
51. I.M. Lifshitz and V.V. Slyozov: *J. Phys. Chem. Solids*, 1961, vol. 19, pp. 35–50.
52. A. Baldan: *J. Mater. Sci.*, 2002, vol. 37, pp. 2171–202.
53. A.J. Ardell: *Acta Metall.*, 1972, vol. 20(1972), pp. 601–9.
54. S.M. He, N.H. van Dijk, M. Paladugu, H. Schut, J. Kohlbrecher, F.D. Tichelaar, and S. van der Zwaag: *Phys. Rev. B*, 2010, vol. 82, p. 174111.
55. E. Pereloma, D. Cortie, N. Singh, G. Casillas, and F. Niessen: *Mater. Res. Lett.*, 2020, vol. 8(9), pp. 341–7.
56. N. Singh, G. Casillas, D. Wexler, C. Killmore, and E. Pereloma: *Acta Mater.*, 2020, vol. 201, pp. 386–402.
57. N. Kamikawa, K. Sato, G. Miyamoto, M. Murayama, N. Sekido, K. Tsuzaki, and T. Furuhara: *Acta Mater.*, 2015, vol. 83, pp. 383–96.